AIAA JOURNAL
Vol. 31, No. 7, July 1993

Analysis of Hypersonic Nozzles Including Vibrational Nonequilibrium and Intermolecular Force Effects

P. W. Canupp,* G. V. Candler,† J. N. Perkins,‡ W. D. Erickson§
North Carolina State University, Raleigh, North Carolina 27695

A computational fluid dynamics technique is developed for the study of high-pressure, axisymmetric hypersonic nozzle flows. The effects of intermolecular forces and vibrational nonequilibrium are included in the analysis. The numerical simulation of gases with an arbitrary equation of state is discussed. Simulations for high-pressure nitrogen nozzles ($p_0 = 138$ MPa) demonstrate that both intermolecular forces and vibrational nonequilibrium affect the flow significantly. These nonideal effects tend to increase the Mach number at the nozzle exit plane. In addition, these effects may introduce weak expansion and compression waves in the nozzle that degrade test section flow quality. Thus, they must be included in the design and analysis of high-pressure hypersonic nozzles.

Nomenclature

A = Jacobian of the x direction inviscid flux vector
A_+, A_- = flux vector Jacobians for the split fluxes
c_p, c_v = specific heats at constant pressure and volume, respectively
E_{tr+rot} = total nonvibrational energy per unit volume
E_{vib} = vibrational energy per unit volume
e_{tr+rot} = translational-rotational energy per unit mass
e_{vib} = vibrational energy per unit mass
$\boldsymbol{F}_I$ = inviscid flux vector in the x direction
$\boldsymbol{F}, \boldsymbol{G}$ = flux vectors in the x and y directions, respectively
h = enthalpy per unit mass
p = pressure
Q_v = vibrational energy transfer rate
q_{vx}, q_{vy} = vibrational heat conduction in the x and y directions, respectively
q_x, q_y = total heat conduction in the x and y directions, respectively
R = gas constant
T = translational-rotational temperature
T_v = vibrational temperature
$\boldsymbol{U}$ = vector of conserved variables
u, v = velocities in the x and y directions, respectively
$\boldsymbol{W}$ = vector of source terms
x, y = Cartesian coordinates
z = compressibility factor
β_i = ith temperature coefficient in the real gas equation of state
θ_v = characteristic temperature of vibration
κ = conductivity of translational-rotational temperature
κ_v = conductivity of vibrational temperature
ρ = density
$\tau_{xx}, \tau_{yy}, \tau_{xy}, \tau_{\theta\theta}$ = stress tensor components
τ_v = vibrational relaxation time
μ = viscosity

Presented as Paper 92-0330 at the AIAA 30th Aerospace Sciences Meeting, Reno, NV, Jan. 6–9, 1992; received June 9, 1992; revision received Oct. 10, 1992; accepted for publication Oct. 16, 1992. Copyright © 1992 by the American Institute of Aeronautics and Astronautics, Inc. All rights reserved.

*Graduate Research Assistant, Department of Mechanical and Aerospace Engineering. Student Member AIAA.

†Assistant Professor, Department of Mechanical and Aerospace Engineering; currently Assistant Professor, Department of Aerospace Engineering and Mechanics, University of Minnesota, Minneapolis, MN 55455. Member AIAA.

‡Professor, Department of Mechanical and Aerospace Engineering. Associate Fellow AIAA.

§Visiting Professor, Department of Mechanical and Aerospace Engineering; currently Chief Scientist, Hypersonic Technology Office, NASA Langley Research Center. Associate Fellow AIAA.

Introduction

COMPUTATIONAL fluid dynamics (CFD) is being used to design hypersonic vehicles. These CFD methods must be validated with available experimental data before they can be used with any measure of certainty. Thus, there is a need for hypersonic wind tunnels that produce uniform flows for validation purposes.

A hypersonic flow may be obtained by allowing a high-pressure and high-temperature gas to expand through a converging-diverging nozzle. This rapid expansion is accompanied by a thick boundary layer in the diverging section. As suggested in Ref. 1, the presence of this thick boundary layer contradicts major assumptions used in the traditional nozzle design technique that iteratively couples a method of characteristics solution to a boundary-layer calculation. This may result in a nozzle geometry that does not yield the design exit Mach number and has poor flow quality in the test section.

In addition to thick boundary layers, the vibrational state of the test gas affects the design of the nozzle geometry.[2] During the expansion, the vibrational energy of the gas is usually frozen. This freezing alters the gas dynamics through changes in both the speed of sound and the ratio of specific heats. For this reason, design techniques for hypersonic nozzles should include thermal nonequilibrium effects.

By increasing the stagnation pressure of these nozzles, the boundary-layer thickness can be reduced. Additionally, a higher stagnation pressure lessens the degree of vibrational nonequilibrium in the nozzle by reducing the relaxation time of the gas. In addition to reducing these nonideal effects, high-pressure hypersonic wind tunnels are desirable since they deliver higher test section Reynolds numbers. Therefore, the need arises for design and analysis tools that can be applied to high-pressure nozzles.

The current research focuses on developing a CFD method that enables the analysis of high-pressure nitrogen nozzles. A general equation of state for nitrogen is introduced that describes its nonideal thermodynamic behavior. Furthermore, vibrational relaxation is included in the analysis. This numerical method is used to simulate the flow in several nozzles to show the effects of intermolecular forces and vibrational nonequilibrium.

Governing Equations

To describe the vibrational nonequilibrium flow, the Navier-Stokes equations are used along with an additional equation that describes the finite-rate energy exchange between translational-rotational and vibrational energy modes. For an axisymmetric flow, these equations take the form[2]

$$\frac{\partial \boldsymbol{U}}{\partial t} + \frac{\partial \boldsymbol{F}}{\partial x} + \frac{1}{y}\frac{\partial y\boldsymbol{G}}{\partial y} = \boldsymbol{W} \tag{1}$$

where

$$\boldsymbol{U} = \begin{pmatrix} \rho \\ \rho u \\ \rho v \\ E_v \\ E_{\text{tr+rot}} \end{pmatrix} \quad \boldsymbol{W} = \begin{pmatrix} 0 \\ 0 \\ 1/y\,(p + \tau_{\theta\theta}) \\ Q_v \\ -Q_v \end{pmatrix}$$

$$\boldsymbol{F} = \begin{pmatrix} \rho u \\ \rho u^2 + p + \tau_{xx} \\ \rho uv + \tau_{xy} \\ E_v u + q_{vx} \\ (E_{\text{tr+rot}} + p + \tau_{xx})\,u + \tau_{xy} v + q_x \end{pmatrix} \tag{2}$$

$$\boldsymbol{G} = \begin{pmatrix} \rho v \\ \rho uv + \tau_{yx} \\ \rho v^2 + p + \tau_{yy} \\ E_v v + q_{vy} \\ (E_{\text{tr+rot}} + p + \tau_{yy})\,v + \tau_{yx} u + q_y \end{pmatrix}$$

The first three equations in Eq. (1) are the continuity and momentum equations for an axisymmetric flow. The fourth equation describes the rate of change of vibrational energy per unit volume. In the final equation, changes in nonvibrational forms of energy are described, and a source term appears to allow energy transfer to the vibrational modes. Treating the vibrational energy in this manner simplifies the application of the computational technique to nonequilibrium flows when including the intermolecular force effects. Thus, the energy described in the final equation is given by

$$E_{\text{tr+rot}} = \rho e_{\text{tr+rot}} + \frac{1}{2}\rho\,(u^2 + v^2) \tag{3}$$

The vibrational energy is a function of vibrational temperature and is obtained for a diatomic gas from the harmonic oscillator model

$$E_v = \rho e_v = \rho R \frac{\theta_v}{e^{\theta_v/T_v} - 1} \tag{4}$$

The source term appearing in the energy equations models the energy exchange that occurs between the translational-rotational and vibrational energy modes. This term is obtained from the Landau-Teller model[3]

$$Q_v = \frac{E_v^*(T) - E_v}{\tau_v} \tag{5}$$

where E_v^* is the vibrational energy associated with temperature T and τ_v is the local relaxation time of the gas which is a function of pressure and temperature.[4]

In the preceding equations, the stresses are related to mean flow gradients through the following constitutive relations:

$$\tau_{xx} = -\mu\left(2\frac{\partial u}{\partial x} - \frac{2}{3}\nabla\cdot\boldsymbol{v}\right)$$

$$\tau_{yy} = -\mu\left(2\frac{\partial v}{\partial y} - \frac{2}{3}\nabla\cdot\boldsymbol{v}\right)$$

$$\tau_{\theta\theta} = -\mu\left(2\frac{v}{y} - \frac{2}{3}\nabla\cdot\boldsymbol{v}\right) \tag{6}$$

$$\tau_{xy} = \tau_{yx} = -\mu\left(\frac{\partial u}{\partial y} + \frac{\partial v}{\partial x}\right)$$

$$\nabla\cdot\boldsymbol{v} = \frac{1}{y}\frac{\partial yv}{\partial y} + \frac{\partial u}{\partial x}$$

Additionally, the heat fluxes are related to temperature gradients by

$$q_x = -\kappa\frac{\partial T}{\partial x} + q_{vx} \qquad q_y = -\kappa\frac{\partial T}{\partial y} + q_{vy} \tag{7}$$

and the vibrational heat fluxes are given by

$$q_{vx} = -\kappa_v\frac{\partial T_v}{\partial x} \qquad q_{vy} = -\kappa_v\frac{\partial T_v}{\partial y} \tag{8}$$

In this study, only laminar flows were investigated. Thus, the viscosity is obtained through Sutherland's law, whereas the thermal conductivity comes from a constant Prandtl number assumption. The vibrational thermal conductivity is a function of the viscosity and vibrational temperature

$$\kappa_v = \mu\frac{\partial e_v}{\partial T_v} \tag{9}$$

Therefore, after specifying the pressure, the previous equations form a closed set.

For the case where vibrational equilibrium is enforced everywhere, the same set of equations may be used with a few modifications. Since $T = T_v$ at all points, the vibrational energy equation may be disregarded. Also, $E_{\text{tr+rot}}$ is replaced by the total energy per unit volume E where

$$E = \rho e_{\text{tr+rot}} + E_v(T) + \frac{1}{2}\rho\,(u^2 + v^2) \tag{10}$$

Finally, the source term in the last equation of Eq. (1) does not appear since there is no source of total energy.

Computational Technique

To solve Eq. (1) numerically, the derivatives are approximated as finite differences and the equation set is integrated in time on a mesh of finite volumes. A steady-state solution is obtained using Gauss-Seidel line relaxation.[5,6]

To account for the intermolecular force effects associated with the large densities, an empirical equation of state developed by Jacobsen et al.[7] for nitrogen is used. This equation gives pressure as a function of temperature and density

$$p = \rho RT + \rho^2\left(\sum_{n=1}^{8}\beta_n\rho^{n-1} + e^{-\gamma\rho^2}\sum_{q=1}^{6}\beta_{q+8}\rho^{2q-1}\right) \tag{11}$$

where γ is a constant, and β_n are temperature-dependent coefficients. Equation (11) is accurate to 0.3% in the typical high-density and high-temperature conditions present in this study. In regions where density and temperature are extremely low, e.g., the nozzle exit, Eq. (11) reduces to the ideal gas equation of state with less than 0.03% error. The accuracy of Eq. (11) was verified numerically by computing a compressibility factor z given by the ratio of actual pressure obtained from Eq. (11) to the pressure predicted by the ideal gas equation of state. In high-pressure regions near the throat and subsonic sections of the nozzle, z is approximately 1.25. For typical low-density and low-temperature regions, ideal gas behavior is recovered with $z = 0.999685$. Thus, Eq. (11) is accurate for all conditions encountered in this study. It is helpful to use z as a measure of the extent to which intermolecular force effects alter the ideal behavior of the gas.

Regarding the CFD method, the use of Eq. (11) has several consequences that need to be addressed. Allowing for a general equation of state alters 1) the flux-vector splitting technique, 2) the evaluation of primitive variables, 3) the calculation of the speed of

sound, and 4) the subsonic inflow boundary conditions. Each of these will be discussed individually.

Flux-Vector Splitting for a Real Gas

The CFD scheme uses a modified form of Steger-Warming flux-vector splitting to accurately simulate the spatial derivatives appearing in Eq. (1).[8–10] Flux-vector splitting ensures that the differencing used in solving Eq. (1) is always upwind, thus respecting the direction of information propagation through the flowfield. This differencing can be achieved for a perfect gas by realizing that the inviscid flux vector $\boldsymbol{F}_I$, for example, can be written as

$$\boldsymbol{F}_I = \frac{\partial \boldsymbol{F}_I}{\partial \boldsymbol{U}} \boldsymbol{U} = A\boldsymbol{U} \tag{12}$$

This is a direct result of the fact that with $p = \rho RT$, $\boldsymbol{F}_I$ is homogeneous of order one in $\boldsymbol{U}$. That is,

$$\boldsymbol{F}_I(\lambda \boldsymbol{U}) = \lambda \boldsymbol{F}_I(\boldsymbol{U}) \tag{13}$$

In this case, the flux Jacobian A may be diagonalized to determine the directions of the flux vectors for the differencing scheme. However, when a general equation of state, such as Eq. (11), is used, $\boldsymbol{F}_I$ is no longer homogeneous in $\boldsymbol{U}$. In this case, we follow the approach taken by Liou et al.[11] and recognize that, for $p = p(\rho,e)$,

$$A = \frac{\partial \boldsymbol{F}_I}{\partial \boldsymbol{U}} = A_e + A_\rho \tag{14}$$

where A_e and A_ρ are matrices containing derivatives of pressure with respect to internal energy and density, respectively. Additionally, we note that with the appropriate choice of A_e as given in Ref. 11,

$$\begin{aligned} \boldsymbol{F}_I &= A_e \boldsymbol{U} \\ &= (A - A_\rho)\boldsymbol{U} \\ &= A\boldsymbol{U} - A_\rho \boldsymbol{U} \\ &= A_+ \boldsymbol{U} + A_- \boldsymbol{U} - A_\rho \boldsymbol{U} \end{aligned} \tag{15}$$

In the last step of Eq. (15), a diagonalization procedure similar to the perfect gas case has been used for the real gas flux Jacobian since it possesses the same eigenvalues as the perfect gas case. Here, $A_+\boldsymbol{U}$ and $A_-\boldsymbol{U}$ represent positive and negative flux vectors, respectively, and are differenced accordingly. The A_ρ has eigenvalues that are zero, and thus the last term may be centrally differenced. Thus, Eq. (15) represents the flux-vector splitting technique for a general equation of state. In diagonalizing the flux Jacobians, pressure and energy derivatives are required. These derivatives must recognize the nonideal description of the gas and will be discussed later.

Calculation of Primitive Variables

The solution of Eq. (1) yields the quantities ρ, ρu, ρv, E_v, and $E_{\text{tr+rot}}$. Given these quantities, the translational-rotational temperature, pressure, vibrational temperature, and speed of sound must be calculated. For a perfect gas this procedure is straightforward. However, because of the nontrivial variation of pressure with density and temperature, an iterative technique must be used for a real gas.

To determine the temperature T, given the quantities in $\boldsymbol{U}$ and the internal energy per unit mass e, where

$$e = \frac{E_{\text{tr+rot}}}{\rho} - \frac{1}{2}\frac{(\rho u)^2 + (\rho v)^2}{\rho^2} \tag{16}$$

we may iterate on the isothermal departure function for internal energy[12]

$$e - e^0 = \left(1 - T\frac{\partial}{\partial T}\right)\int_0^\rho \frac{p - \rho RT}{\rho^2}\, d\rho \tag{17}$$

where $e^0 = (5/2)RT$ is the ideal gas translational-rotational energy. By substituting the pressure expression given in Eq. (11) into Eq. (17), the right-hand side of Eq. (17) becomes a function of density and temperature only. Thus, this equation may be iterated for the translational-rotational temperature using a Newton-Raphson method. Pressure can then be calculated directly from Eq. (11). Finally, the vibrational temperature is obtained from Eq. (4).

Calculation of the Speed of Sound

The speed of sound is used extensively in the CFD algorithm. Since it appears in the eigenvalues of the flux Jacobians, its correct calculation is critical in determining the directions of the flux vectors in the flux-vector splitting procedure. The speed of sound in the gas a can be determined in the derivation of the split flux vectors and is given by

$$\begin{aligned} \rho a^2 = {} & \rho \frac{\partial p}{\partial \rho} + \rho u \frac{\partial p}{\partial \rho u} + \rho v \frac{\partial p}{\partial \rho v} + E_v \frac{\partial p}{\partial E_v} \\ & + (E_{\text{tr+rot}} + p)\frac{\partial p}{\partial E_{\text{tr+rot}}} \end{aligned} \tag{18}$$

where these derivatives require that p be expressed in terms of the quantities found in $\boldsymbol{U}$. These derivatives are also needed to diagonalize the flux Jacobians. Since Eq. (11) does not lend itself to simple algebraic manipulation, we use the fact that $p = p(\rho,e)$ to obtain the required derivatives. For example,

$$\left.\frac{\partial p}{\partial \rho}\right|_U = \left.\frac{\partial p}{\partial \rho}\right|_e + \left.\frac{\partial p}{\partial e}\right|_\rho \left.\frac{\partial e}{\partial \rho}\right|_U \tag{19}$$

and using Eq. (16),

$$\left.\frac{\partial p}{\partial \rho}\right|_U = \left.\frac{\partial p}{\partial \rho}\right|_e + \frac{1}{\rho}\left.\frac{\partial p}{\partial e}\right|_\rho \left(u^2 + v^2 - \frac{E_{\text{tr+rot}}}{\rho}\right) \tag{20}$$

Although the explicit function $p = p(\rho,e)$ is unknown, its derivatives can be calculated using Eq. (11) and

$$\left.\frac{\partial p}{\partial \rho}\right|_e = \frac{1}{c_v}\left(c_p \left.\frac{\partial p}{\partial \rho}\right|_T - \frac{p}{\rho^2}\left.\frac{\partial p}{\partial T}\right|_\rho\right) \tag{21}$$

and

$$\left.\frac{\partial p}{\partial e}\right|_\rho = \frac{1}{c_v}\left.\frac{\partial p}{\partial T}\right|_\rho \tag{22}$$

For a real gas, these may be calculated from their definitions along with Eq. (17),

$$c_v \equiv \left.\frac{\partial e}{\partial T}\right|_\rho = \frac{5}{2}R - T\frac{\partial^2}{\partial T^2}\int_0^\rho \frac{p - \rho RT}{\rho^2}\, d\rho \tag{23}$$

and

$$c_p \equiv \left.\frac{\partial h}{\partial T}\right|_p = \left.\frac{\partial}{\partial T}\left(e + \frac{p}{\rho}\right)\right|_p = c_v + \frac{T}{\rho^2}\frac{(\partial p/\partial T)_\rho^2}{(\partial p/\partial \rho)_T} \tag{24}$$

A similar approach is used for calculating the remaining derivatives in Eq. (18). Also needed in the flux-vector splitting are derivatives of translational-rotational energy with respect to the variables ρ, u, v, e_v, and p. These derivatives are obtained through a procedure similar to that outlined earlier.

Real Gas Subsonic Inflow Boundary Conditions

Boundary conditions for a subsonic inflow are well known for a perfect gas. For a real gas, these must be reformulated to relax the ideal gas assumption. In the real gas case, a relationship governing properties for the outgoing characteristic at the inflow boundary is used. This is identical to that used for a perfect gas and is given by

$$\frac{\partial p}{\partial t} - \rho a \frac{\partial u}{\partial t} = -(u - a)\left(\frac{\partial p}{\partial x} - \rho a \frac{\partial u}{\partial x}\right) \tag{25}$$

Also, since pressure and velocity are related by

$$\frac{\partial p}{\partial u} = -\rho u \tag{26}$$

we can write an update equation for the velocity at the inflow points as

$$\frac{\partial u}{\partial t} = \frac{(u-a)}{\rho\,(u+a)}\left(\frac{\partial p}{\partial x} - \rho a \frac{\partial u}{\partial x}\right) \tag{27}$$

Using the previous expression and assuming that the flow enters parallel to the centerline, i.e., $v = 0$, we can obtain updated values for velocity at the inflow points. To relate properties in the interior to the inflow points, the right-hand side of Eq. (27) is evaluated at the given time level, whereas the derivative on the left-hand side gives the updated velocity. The assumption that the flow is parallel to the centerline does not introduce significant error since the kinetic energy of the gas is negligible compared with the internal energy at the inflow. Because the flow is adiabatic between the stagnation chamber and the first set of grid points, the enthalpy at each inflow point may be calculated according to

$$h^{n+1} = h_0 - \frac{1}{2}(u^{n+1})^2 \tag{28}$$

where the $n + 1$ superscript denotes updated values at the boundary. For a reversible, hence isentropic, flow up to the first grid points, the density and temperature may be calculated by simultaneous iteration of

$$h^{n+1} = e(\rho^{n+1}, T^{n+1}) + \frac{p(\rho^{n+1}, T^{n+1})}{\rho^{n+1}} \tag{29}$$

and

$$h^{n+1} - h_0 = \frac{p^{n+1} - p_0}{\rho_0} \tag{30}$$

Upon calculation of density and temperature, the pressure and inflow energy may be calculated. In this way, the change in $\boldsymbol{U}$ may be calculated at the inflow plane and used in the solution update.

Results and Discussion

In this section we discuss the results of a grid resolution study. We then compare CFD results to those of a method-of-characteristics analysis for an inviscid nozzle. Finally, the effects of intermolecular forces and vibrational nonequilibrium are assessed through simulations of the flow in two different nozzle contours designed using the method-of-characteristics/boundary-layer technique.[13–15] These nozzles were designed for the same operating conditions with an exit Mach number of 14 and stagnation conditions of p_o = 137.9 MPa and T_0 = 1889 K. These are proposed stagnation conditions for the NASA Langley Experimental Hypersonics Branch nitrogen facility. Both of the nozzle contours were designed using a laminar boundary layer, an equilibrium gas, and a specified wall temperature distribution. The wall temperature distribution was based on estimates provided by NASA Langley Research Center based on their backside wall cooling capabilities. This temperature was specified on the nozzle wall and held fixed during the CFD calculations. The difference between the two nozzles is that one was designed assuming a thermally perfect gas, whereas the other was designed for a real gas. The specifications of both nozzles are given in Table 1.

The CFD solutions were computed from the subsonic region (approximately 7 throat radii upstream of the throat) to the exit of the nozzle. The wall geometry for the subsonic section was a 7.62-cm radius circular arc for each nozzle. At the first set of grid points, the pressure was approximately 95% of the stagnation pressure, and the Mach number was generally 0.2.

Table 1 Nozzle geometries

	Perfect gas	Real gas
Throat radius, m	3.332×10^{-3}	4.093×10^{-3}
Exit radius, m	2.540×10^{-1}	2.540×10^{-1}
Length, m	3.761	3.710
Maximum expansion angle, deg	20	20

Grid Resolution Study

The numerical method was used to compute the steady-state solution in a high-pressure nozzle for an equilibrium perfect gas using different axial and radial mesh sizes. The thermally perfect gas nozzle discussed earlier was used for this study. We found that the axial mesh spacing in the low-supersonic region where the flow is expanding rapidly greatly affects the Mach number predicted at the nozzle exit plane. For this nozzle, a mesh spacing of Δx = 0.127 cm was sufficiently fine for resolving the flow. An axial grid spacing twice as fine resulted in the same centerline Mach number distribution. This can be seen in Fig. 1, which is a plot of the centerline Mach number for the three different axial mesh spacings investigated. In the region where the gas is expanding less quickly, a coarser mesh spacing may be used. In this case Δx = 0.254 cm was used 60 cm beyond the throat. This results in approximately grid points in the axial direction.

Changes in the radial mesh resolution have less effect on the nozzle flow. However, if the mesh is too coarse in the boundary layer, a set of compression waves may be generated at the nozzle wall. These waves propagate to the exit plane of the nozzle and significantly affect the core flow. For finer meshes, these waves do not appear. This can be seen in Fig. 2, which shows centerline Mach numbers for four different radial grid sizes. For the coarse mesh cases, the nonphysical waves impinge on the centerline at about 50% of the nozzle length. For the 160 and 190 grid point cases, these waves do not appear. For the case considered, 160 grid

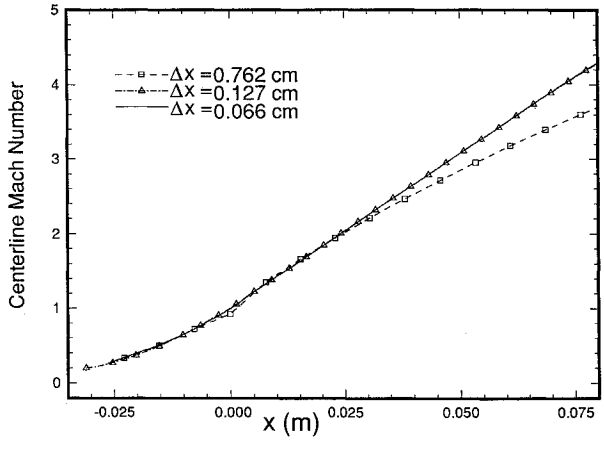

Fig. 1 Centerline Mach number distributions for three different axial mesh spacings for the equilibrium perfect gas model.

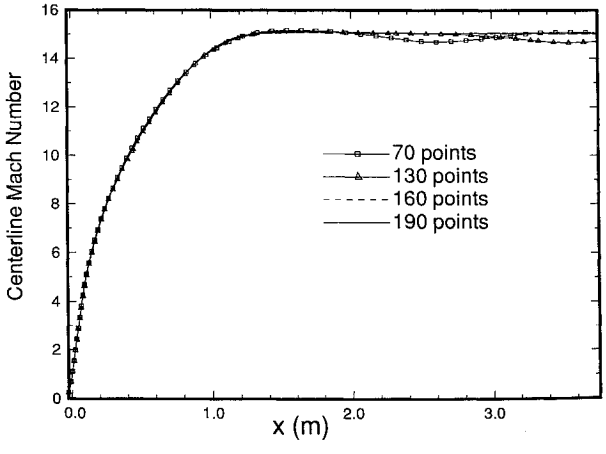

Fig. 2 Centerline Mach number distributions for four different radial mesh spacings for the equilibrium perfect gas model.

points in the radial direction were sufficient to yield a grid-converged solution. Of these points, 70 were located in the core flow region, whereas the remaining points were exponentially stretched to a minimum mesh spacing of 1/2000 of the local nozzle radius.

Inviscid Nozzle Results

To validate the numerical method, a nozzle was designed without a boundary layer using an equilibrium perfect gas equation of state. The design exit Mach number was 14. The CFD method without viscous terms was then used to compute the flow in this nozzle. In this simulation, the CFD resulted in a nearly uniform exit Mach number distribution within 0.02 of the design Mach number.

Viscous Nozzle Results

Six different viscous simulations were performed to show the effects of intermolecular forces and vibrational nonequilibrium. First we will discuss results obtained with the nozzle contour designed using an equilibrium perfect gas equation of state.

Consider Fig. 3, which is a plot of the centerline Mach numbers for the vibrational equilibrium perfect gas and real gas models in the equilibrium perfect gas nozzle. The perfect gas calculation yields an exit Mach number of 15.1, considerably higher than the design. This difference must be attributed to the treatment of the boundary layer in the design code since the previous example

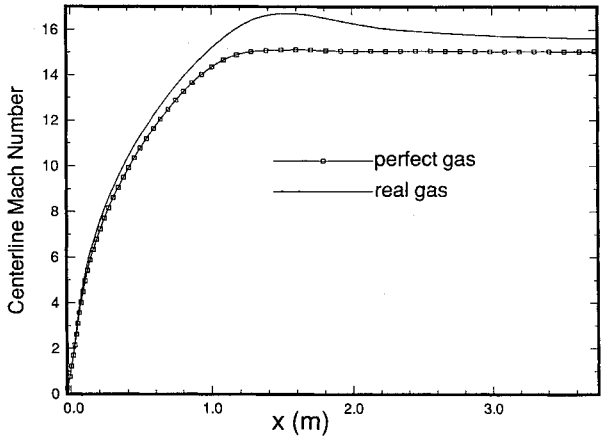

Fig. 3 Centerline Mach number distributions for equilibrium perfect gas and real gas models in the laminar, equilibrium perfect gas nozzle. Design Mach number is 14; p_0 = 137.9 MPa, and T_0 = 1889 K.

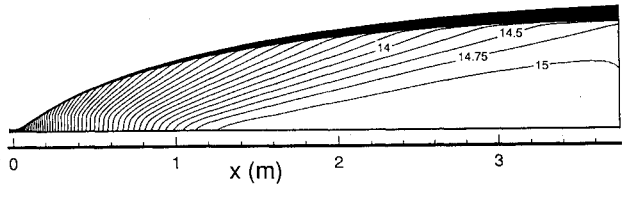

Fig. 4 Mach number contours for the equilibrium perfect gas model in the laminar, equilibrium perfect gas nozzle. Nozzle radius has been scaled by a factor of 3. Design Mach number is 14; p_0 = 137.9 MPa, and T_0 = 1889 K.

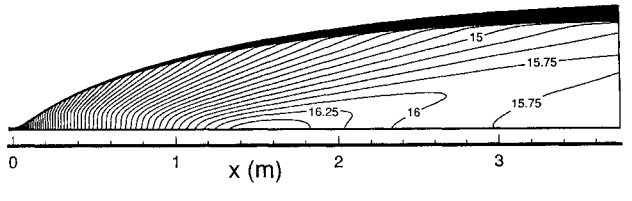

Fig. 5 Mach number contours for the equilibrium real gas model in the laminar, equilibrium perfect gas nozzle. Nozzle radius has been scaled by a factor of 3. Design Mach number is 14; p_0 = 137.9 MPa, and T_0 = 1889 K.

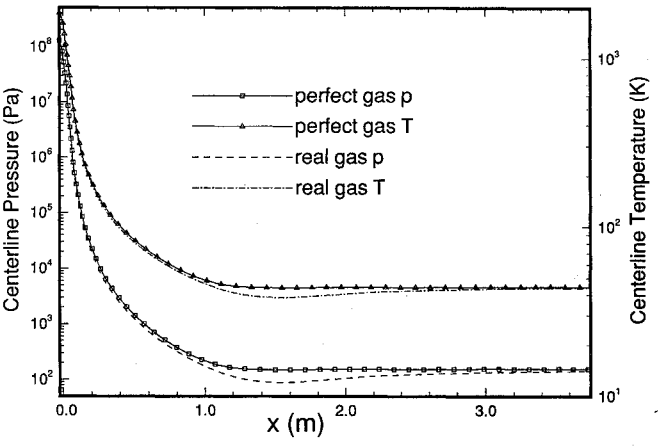

Fig. 6 Centerline pressure and temperature distributions for equilibrium perfect gas and real gas models in the laminar, equilibrium perfect gas nozzle. Design Mach number is 14; p_0 = 137.9 MPa, and T_0 = 1889 K.

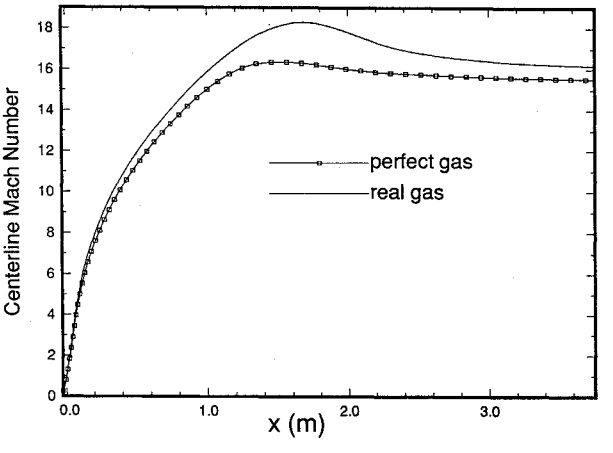

Fig. 7 Centerline Mach number distributions for nonequilibrium perfect gas and real gas models in the laminar, equilibrium perfect gas nozzle. Design Mach number is 14; p_0 = 137.9 MPa, and T_0 = 1889 K.

shows that there is excellent agreement between the CFD and the design technique if no boundary layer is included. We would expect the CFD rather than the design technique to give the correct result, since the CFD includes all viscous terms, whereas the design technique relies on an approximate coupling of the inviscid flow to the boundary layer. Thus, the design technique does not work well for this type of nozzle. This observation is consistent with those of Ref. 1 which suggest that, to obtain an accurate nozzle design with the method-of-characteristics/boundary-layer approach, the design exit Mach number should not exceed 8. Now if we compare the perfect gas and real gas results, we see that the real gas equation of state yields an even higher exit Mach number of 15.7. In addition, there is a significant overexpansion of the gas to a peak Mach number of 16.7. The Mach number contours for these cases are shown in Figs. 4 and 5. In these plots, the radial dimension has been expanded by a factor of 3 for clarity. Figure 4, which is for the perfect gas model, shows a uniform expansion to a Mach number of 15. The Mach 15 contour bends downward near the exit plane. This shows that a weak wave reflects from the centerline and crosses the nozzle exit plane. For the real gas equation of state, shown in Fig. 5, the gas overexpands and then undergoes recompression to the nozzle exit. A compression wave originates at the wall in the low supersonic region of the nozzle and propagates to the centerline. This wave then reflects from the centerline and passes through the nozzle exit plane. Also, note that the real gas case has less core flow at the exit. This is due to the larger Mach number (hence thicker boundary layer) predicted by the real gas analysis. Consider Fig. 6, which is a plot of the centerline pressure

and temperature for these two cases. Note that the pressure and temperature are essentially the same for both gas models in the throat region. The differences occur in the region where the overexpansion occurs. This is a result of information that has propagated to the centerline from the upstream high-pressure region. Thus, although the gas is locally at a low pressure, its dynamics are affected by intermolecular forces in the high-pressure region. This shows that, although the pressure on the centerline in the throat region is not significantly different in the two cases, the gas dynamics are changed by the nonideal effects. These differences can be attributed to the additional flux term $A_\rho U$ appearing in Eq. (15). It should be noted that in the throat region of the nozzle, these additional terms can comprise as much as 25% of the total inviscid flux. So, by including intermolecular forces in the flux-vector splitting scheme, we include important nonideal effects. The pressure and temperature at the exit of the nozzle are nearly the same for the two models. However, this agreement is probably spurious in light of the differences in the upstream gas dynamics. From these comparisons, it is clear that intermolecular force effects must be included in an analysis of the flow in high-pressure nozzles.

Next we will consider the vibrational nonequilibrium simulations for the laminar, equilibrium perfect gas nozzle. Referring to Fig. 7, which shows the distribution of the Mach number along the centerline, we see that CFD predicts exit Mach numbers of 15.5 and 16.2 for the perfect and real gas models, respectively. Thus, in comparison with Fig. 3, vibrational nonequilibrium has the effect of further increasing the Mach numbers in the nozzle. For nonequilibrium, the perfect gas model results in an overexpansion to a Mach number of 16.3, whereas the real gas peaks at 18.3. This overexpansion is again apparent in the Mach number contour plots shown in Figs. 8 and 9. These two plots are similar to the equilibrium cases with higher Mach numbers caused by the nonequilibrium effects. It should be noted that the speed of sound used to determine the Mach number in the nonequilibrium cases is given by Eq. (18). This is computed as the frozen speed of sound for the nonequilibrium cases. Thus, the higher Mach numbers are primarily due to the fact that energy is frozen in the vibrational modes. In Fig. 9, the weak waves are clearly seen to reflect from the centerline after the overexpansion. These waves then propagate into the exit plane of the nozzle, thereby contaminating the test section flow. It is clear from these results that both intermolecular force and vibrational nonequilibrium effects significantly affect the flow in high-pressure nozzles. It should be noted that we would expect the nonequilibrium real gas model to most closely approximate the actual nozzle flow. Thus, the calculations show that if a high-pressure Mach 14 nozzle is designed using an equilibrium perfect gas, one should expect to obtain an exit Mach number of 16.2, and waves would exist in the nozzle test section.

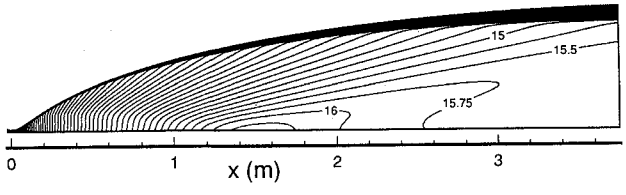

Fig. 8 Mach number contours for the nonequilibrium perfect gas model in the laminar, equilibrium perfect gas nozzle. Nozzle radius has been scaled by a factor of 3. Design Mach number is 14; p_0 = 137.9 MPa, and T_0 = 1889 K.

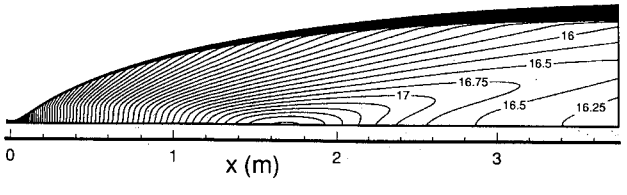

Fig. 9 Mach number contours for the nonequilibrium real gas model in the laminar, equilibrium perfect gas nozzle. Nozzle radius has been scaled by a factor of 3. Design Mach number is 14; p_0 = 137.9 MPa, and T_0 = 1889 K.

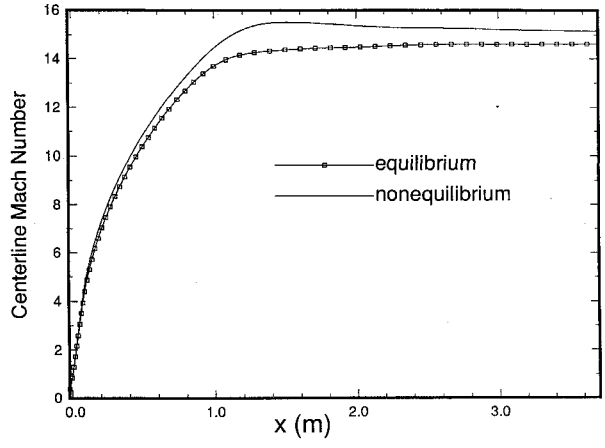

Fig. 10 Centerline Mach number distributions for equilibrium and nonequilibrium real gas models in the laminar, equilibrium real gas nozzle. Design Mach number is 14; p_0 = 137.9 MPa, and T_0 = 1889 K.

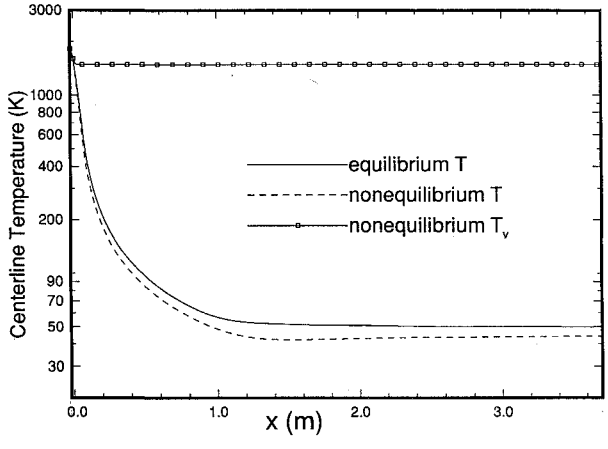

Fig. 11 Centerline temperature distributions for equilibrium and nonequilibrium real gas models in the laminar, equilibrium real gas nozzle. Design Mach number is 14; p_0 = 137.9 MPa, and T_0 = 1889 K.

Now consider the nozzle that was designed using a vibrational equilibrium real gas equation of state. Thus, intermolecular force effects are accounted for in this design. The design conditions for this nozzle are the same as those used for the perfect gas nozzle.

Shown in Fig. 10 are centerline Mach number distributions for equilibrium and nonequilibrium simulations with a real gas equation of state. It can be seen that the equilibrium gas yields an exit Mach number of 14.6, whereas the nonequilibrium gas results in 15.2. Additionally, the extent of vibrational nonequilibrium can be seen in Fig. 11, which is a plot of temperature distributions along the nozzle centerline for both cases. The vibrational temperature freezes near the throat at 1483 K for the nonequilibrium case. Because of this freezing, the translational-rotational temperature is slightly lower than the equilibrium temperature in the remainder of the nozzle. Figure 12 shows the Mach number contours for the equilibrium case. An expansion wave appears at the nozzle wall and impinges on the centerline at about 60% of the nozzle length. This wave allows a continued expansion to the nozzle exit. For the nonequilibrium case, an overexpansion to Mach 15.5 occurs as can be seen in Fig. 13. This expansion is then followed by a slight recompression to the exit Mach number of 15.2. In this case, the compression wave reflects into the exit plane. Comparing Fig. 13 with Fig. 9, it can be seen that by including intermolecular force effects in the nozzle design process, a better flow quality is obtained in the nozzle exit plane. However, because of the inadequacies of the design technique and the presence of vibrational nonequilibrium, the simulations predict exit Mach numbers that are higher than design.

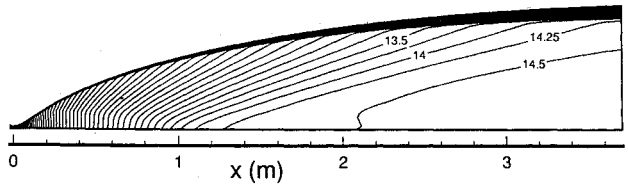

Fig. 12 Mach number contours for the equilibrium real gas model in the laminar, equilibrium real gas nozzle. Nozzle radius has been scaled by a factor of 3. Design Mach number is 14; p_0 = 137.9 MPa, and T_0 = 1889 K.

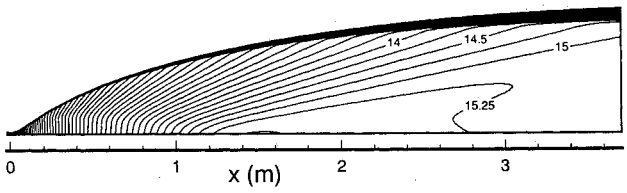

Fig. 13 Mach number contours for the nonequilbrium real gas model in the laminar, equilibrium real gas nozzle. Nozzle radius has been scaled by a factor of 3. Design Mach number is 14; p_0 = 137.9 MPa, and T_0 = 1889 K.

The simulations just discussed were performed on a Cray Y-MP. For the 923×160 grid used in the equilibrium perfect gas cases, a steady-state solution required 46 min of CPU time. This case cost 3×10^{-5} s/grid point/iteration. This cost increased to 4.5×10^{-5} s/grid point/iteration for the equilibrium real gas simulation. For the nonequilibrium perfect gas case, the code required 4×10^{-5} s/grid point/iteration. The vibrational nonequilibrium real gas case required 5.5×10^{-5} s/grid point/iteration. It should be noted that the above performance times indicate the cost associated with each gas model.

Conclusions

A computational fluid dynamics method has been developed to simulate the flow of vibrationally relaxing, high-pressure nitrogen. A general equation of state was used. Modifications to the flux-vector splitting technique, the method for calculating the primitive variables and the speed of sound, and the treatment of the subsonic inflow boundary conditions were made. Grid resolution studies and comparisons with an inviscid flow were performed to validate the computational method. The technique was then used to simulate the flow in two different high-pressure hypersonic nozzles. These nozzles were designed using a method-of-characteristics/boundary-layer technique. All of the simulations result in an exit Mach number different than design. This is likely due to problems associated with coupling the boundary layer to the inviscid flow in the nozzle design technique. The simulations show that intermolecular force effects and vibrational nonequilibrium increase the exit Mach number. These effects cause an overexpansion of the gas, resulting in a pocket of high Mach number flow at about 40% of the nozzle length. The nozzle designed with an equilibrium perfect gas equation of state yields a poor quality of flow due to expansion and compression waves crossing the nozzle exit plane. The nozzle designed with an equilibrium real gas equation of state has superior flow quality and a Mach number closer to design conditions. These results show that high-pressure nozzles must be designed with the correct thermodynamic representation of the gas.

Acknowledgments

Support for this work was provided by NASA under Grant NAGW-1331 to the Mars Mission Research Center at North Carolina State University. Additional funding was supplied by the North Carolina Space Grant Consortium. Patrick Canupp received support from a U.S. Department of Energy Computational Science Graduate Fellowship. Computer time was provided by the North Carolina Supercomputing Center.

References

[1]Benton, J., Perkins, J., and Edwards, A., "Limitations of the Method of Characteristics When Applied to Axisymmetric Hypersonic Nozzle Design," AIAA Paper 90-0192, Jan. 1990.

[2]Candler, G. V., and Perkins, J. N., "Effects of Vibrational Nonequilibrium on Hypersonic Nozzle Design," AIAA Paper 91-0297, Jan. 1991.

[3]Vincenti, W. G., and Kruger, C. H., Jr., *Introduction to Physical Gas Dynamics*, Krieger Publishing, Malabar, FL, 1965.

[4]Millikan, R. C., and White, D. R., "Systematics of Vibrational Relaxation," *Journal of Chemical Physics*, Vol. 39, No. 12, 1963, pp. 3209–3213.

[5]MacCormack, R. W., "Current Status of Numerical Solutions of the Navier-Stokes Equations," AIAA Paper 85-0032, Jan. 1985.

[6]Candler, G. V., "The Computation of Weakly Ionized Hypersonic Flows in Thermo-Chemical Nonequilibrium," Ph.D. Thesis, Stanford Univ., Stanford, CA, 1988.

[7]Jacobsen, R. T., Stewart, R. B., McCarty, R. D., and Hanley, H. J. M., "Thermophysical Properties of Nitrogen from the Fusion Line to 3500 R (1944 K) for Pressures to 150,000 psia (10342×10^5 N/m^2)," National Bureau of Standards, NBS TN 648, Boulder, CO, Dec. 1973.

[8]Steger, J., and Warming, R. F., "Flux Vector Splitting of the Inviscid Gasdynamics Equations with Application to Finite Difference Methods," NASA TM-78605, 1979.

[9]MacCormack, R. W., and Candler, G. V., "The Solution of the Navier-Stokes Equations Using Gauss-Seidel Line Relaxation," *Computers and Fluids*, Vol. 17, No. 1, 1989, pp. 135–150.

[10]Van der Vegt, J. J. W., "Assessment of Flux Vector Splitting for Viscous Compressible Flows," AIAA Paper 91-0242, Jan. 1991.

[11]Liou, M. S., Van Leer, B., and Shuen, J. S., "Splitting of Inviscid Fluxes for Real Gases," NASA TM-100856, April 1988.

[12]Modell, M., and Reid, R., *Thermodynamics and its Applications*, Prentice-Hall, Englewood Cliffs, NJ, 1983.

[13]Johnson, C. B., "Real-Gas Effects on Hypersonic Nozzle Contours with a Method of Calculation," NASA TN D-1622, April 1963.

[14] Johnson, C. B., and Boney, L. R., "A Method for Calculating Real-Gas Two-Dimensional Nozzle Contour Including the Effects of Gamma," NASA TM X-3243, Sept. 1975.

[15]Anderson, E. C., and Lewis, C. H., "Laminar or Turbulent Boundary-Layer Flows of Perfect Gases or Reacting Gas Mixtures in Chemical Equilibrium," NASA CR-1893, 1971.